AIAA Aviation Forum and ASCEND co-located Conference Proceedings
29 July - 2 August 2024, Las Vegas, Nevada
AIAA AVIATION FORUM AND ASCEND 2024
10.2514/6.2024-4560

Optimizing Optical Emission Measurements on the Varda Hypersonic Testbed Vehicle

Marat Kulakhmetov[1] and Robert Alviani[2]
Varda Space Industries, El Segundo, CA, 90245

Ashwin P. Rao,[3] Vanessa J. Murray,[4] Jonah B. Taylor,[5] Jason G. Seik,[6] and Erin I. Vaughan[7]
Air Force Research Laboratory, Kirtland AFB, NM, 87117

Varda Space Industries, in partnership with the Air Force Research Laboratory (AFRL), will reenter the Varda Hypersonic Testbed vehicle in late 2024. This mission will be equipped with the Optical Sensing of Plasmas in the REentry Environment (OSPREE) payload. OSPREE is a spectrometer which will record in situ measurements of the flowfield during re-entry. Herein, we present the methodology used to determine the detector exposure time for the spectrometer. The three-dimensional computational fluid dynamics (CFD) code Langley Aerothermodynamic Upwind Relaxation Algorithm (LAURA) was employed to simulate the hypersonic flowfield chemistry of the vehicle. Flowfield species chemical concentrations, pressures, and temperatures were produced using LAURA at various trajectory locations. Two specific trajectory points, corresponding to peak heating and peak dynamic pressure, were simulated for angles of attack of 0° and 20° and with 5 species and 11 species air-chemistry models. The CFD flowfield solutions along a predetermined optical line of sight (LOS) were analyzed using the radiative transport and spectral solver Nonequilibrium Air Radiation (NEQAIR) to generate simulated optical emission spectra of the plasma sheath. The choice of air chemistry model had minimal impact on the calculated total spectral radiance and corresponding spectrometer intensity at each of the trajectory points, although additional atomic transitions were observed using the 11 species model. The different trajectory points, however, significantly affected the calculated radiance, which indicates that the spectrometer exposure time may need to be varied over the course of reentry. This research is critical to modeling the response of spectral sensing payloads and defining key operating parameters, such as spectrometer exposure time.

I. Nomenclature

α	=	angle of attack [°]
T	=	temperature [K]
T_{tr}	=	translational temperature [K]
T_r	=	rotational temperature [K]
T_v	=	vibrational temperature [K]

II. Introduction

High-enthalpy hypersonic flows are generated by high-speed vehicles and extraterrestrial objects such as asteroids or space debris as they penetrate Earth's atmosphere. An improved understanding of such flows will enable the development of safer and more cost-effective hypersonic vehicles [1], support assessment of reentry debris risk by government regulators [2], and enhance understanding of the impact of meteors and asteroids on the geological evolution of Earth

[1]Head of Analysis & Hypersonics, Varda Space Industries, El Segundo, CA, 90245
[2]Aerodynamics Engineer, Varda Space Industries, El Segundo, CA, 90245
[3]Physicist, Space Vehicles Directorate, Air Force Research Laboratory, Kirtland AFB, NM, 87117
[4]Chemist, Space Vehicles Directorate, Air Force Research Laboratory, Kirtland AFB, NM, 87117
[5]Plasma Physicist, Space Vehicles Directorate, Air Force Research Laboratory, Kirtland AFB, NM, 87117
[6]Physicist, Space Vehicles Directorate, Air Force Research Laboratory, Kirtland AFB, NM, 87117
[7]Nuclear Engineer, Space Vehicles Directorate, Air Force Research Laboratory, Kirtland AFB, NM, 87117

[3]. Despite over 60 years of high-velocity flight experience, hypersonic flows still remain poorly understood for a range of reasons. First, current ground test facilities are incapable of producing flows that simultaneously match Mach number, Reynolds number, flowfield enthalpy, freestream composition, and test duration corresponding to hypersonic flight conditions above Mach 12. Second, many chemistry models used to predict flows at temperatures above 15,000K (as is needed for flight at Mach > 20) are anchored to laboratory measurements at temperatures of only 5000 K[4, 5], not validated by real flight data. Furthermore, the development, operation, and instrumentation of hypersonic vehicles has historically been expensive. Using these systems solely for high-risk hypersonic flight experiments is not yet economically feasible.

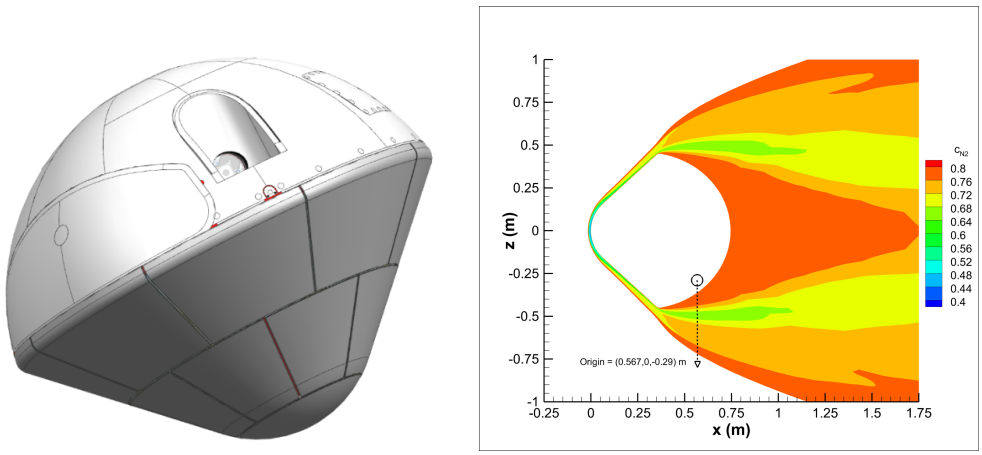

(a) **(b)**

Fig. 1 a) Varda Hypersonic Testbed vehicle and b) CFD flowfield and LOS vector.

Varda Space Industries has developed a reentry capsule to return commercial materials manufactured in low-earth orbit (LEO). On February 21, 2024, Varda's W-1 capsule became the first U.S. commercial spacecraft to reenter and land on American soil. The low cost and high launch cadence planned for these capsule returns makes them an ideal hypersonic experimentation testbed. The U.S. Air Force (USAF) awarded a contract to Varda to expand the capability of their commercial vehicle to support hypersonic flight testing. This 1 m diameter hypersonic testbed vehicle, shown in Fig. 1a, will be used to study aerothermodynamics, develop advanced thermal protection systems (TPS), and flight qualify various emerging technologies.

The first USAF-Varda hypersonic test flight is scheduled for the Fall of 2024. This mission will include the Optical Sensing of Plasmas in the Reentry Environment (OSPREE) payload, which is an optical emission spectroscopy (OES) sensor designed to measure electronic deexciation emission from energetic plasma flows. It is difficult to develop external sensors to probe hypersonic flowfields without perturbing the vehicle aerodynamics or sustaining damage at peak heating flight conditions. OES offers a way to probe the high enthalpy flows non-intrusively from a safe location within the vehicle. These spectral measurements could provide direct information about flow thermal states, species densities, and chemical composition of the reentry flowfield. This data is necessary to validate high-fidelity computational fluid dynamic (CFD) and direct simulation Monte Carlo (DSMC) simulations, improve high enthalpy air kinetics models, and understand the ablation chemistry from the vehicle TPS [6–8]. Furthermore, the spectral measurements from this flight will inform the development and test of more advanced optical sensing payloads.

The authors are aware of only two previous public attempts to make direct spectral measurements at hypersonic flight conditions. The first available measurements were made on the Bow Shock Ultra Violet -2 (BSUV-2) sounding rocket flight in 1991 [9]. This flight reached a constant velocity of 5.1 km/s (Mach 16) at altitudes between 62 and 115 km. BSUV-2 vehicle carried an UV/VIS spectrometer that was capable of sampling between 200-400 nm, and pyrometers sampling at 215 nm, 230 nm, and 310 nm. This flight produced the most comprehensive reentry spectral emissions data currently publicly available to researchers and has been used to calibrate many CFD and DSMC models [10–12]. The second vehicle developed for the purpose of making spectral measurements at hypersonic conditions was ESA's EXPERT [13]. EXPERT was a reentry capsule with a 0.55m nose radius that was supposed to fly on a converted ICBM, Volna [14, 15]. The vehicle was designed to fly a ballistic trajectory with a peak Mach number of 21 taking emission measurements between 200 nm and 800 nm. Unfortunately this vehicle did not fly after its original launch

provider withdrew from the effort. Varda's first hypersonic test flight mission will be the third attempt to make spectral measurements at hypersonic conditions. Varda's test flight is expected to reach flight velocities in excess of 8 km/s when it hits the upper atmosphere at a flight path angle of approximately -4 deg. The data generated by this flight will significantly extend the dataset previously generated by BSUV-2.

The OSPREE payload flying on the Varda hypersonic testbed is based on a modified Ocean Insight HR2 spectrometer. The payload integrated into the testbed is shown in Fig. 2. The spectrometer has been modified to survive launch, reentry, and in-space environments. These modifications will be discussed in a later publication. The shock-layer emissions are collected along a line of sight (LOS) perpendicular to the vehicle nose and centered at the aft body optical window. This LOS has an origin at (0.567, 0, -0.29) m and is shown as a dashed line in Fig. 1b. A collimator resides behind a quartz window in a pocket on the aft body; this helps manage heat loads to the window and ensures survivability. The collimator is connected to the spectrometer via a fiber optic cable, as shown in Fig. 2b.

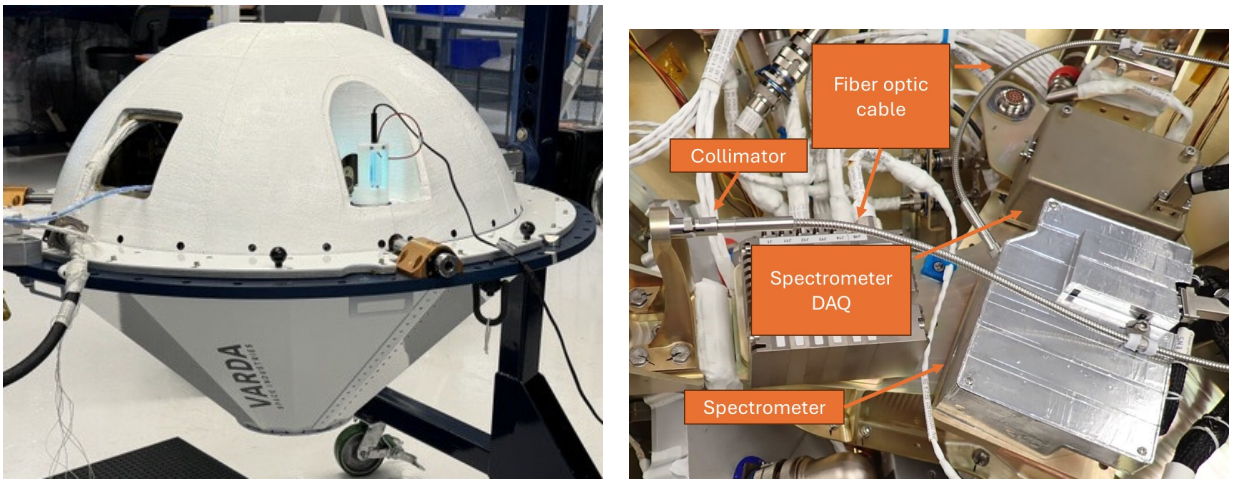

(a) **(b)**

Fig. 2 a) Varda capsule in assembly and b) OSPREE payload installed in capsule.

Pre-flight flowfield spectral radiance emissions have been computed in order to calibrate OSPREE and help ensure that the flight scientific objectives will be met. OSPREE's detector exposure time is programmed in software before launch, necessitating spectral radiance predictions correlated to detector response to ensure correct exposure time for signal recording. Furthermore, the flight test seeks to measure dynamic flowfield chemistry changes to validate nonequilibrium chemistry models. This necessitated a fundamental understanding of the atomic and molecular species that emerge during reentry. To achieve these objectives, we simulated the reentry shock layer using the Langley Aerothermodynamic Upwind Relaxation Algorithm (LAURA) CFD code [16]. These simulations implemented 5 species and 11 species air-chemistry models with both thermal equilibrium (single temperature) and thermal nonequilibrium (two temperature). The thermochemical properties for each flowfield solution were extracted along the optical LOS and used with the Nonequilibrium Air Radiation (NEQAIR) solver [17] to calculate expected VIS-NIR emissions. This paper discusses these CFD flowfield simulations, the methodology for determining spectral radiance, the detector response analysis, and the potential impact of this test to validate hypersonic aerothermodynamic models in high Mach regimes.

III. Image Data From First Reentry Mission

Varda's first atmospheric reentry mission took place in February 2024. This reentry capsule was outfitted with many sensors, include a camera positioned behind the separation pocket window along the same LOS as the OSPREE. A few frames from this footage, which has been released publicly, are highlighted in Fig. 3 [18]. Each frame is marked by the time after capsule separation from the satellite bus, along with corresponding altitude and velocity determined during post-flight trajectory reconstruction. Radiant emissions in Fig.3 first manifested when the vehicle was at Mach 29 at an altitude of 95 km and persisted until the vehicle slowed down to Mach 17 at an altitude of 50 km. Based on this image data, detectable emissions are expected to transition from a purple glow to a red glow and then back to a

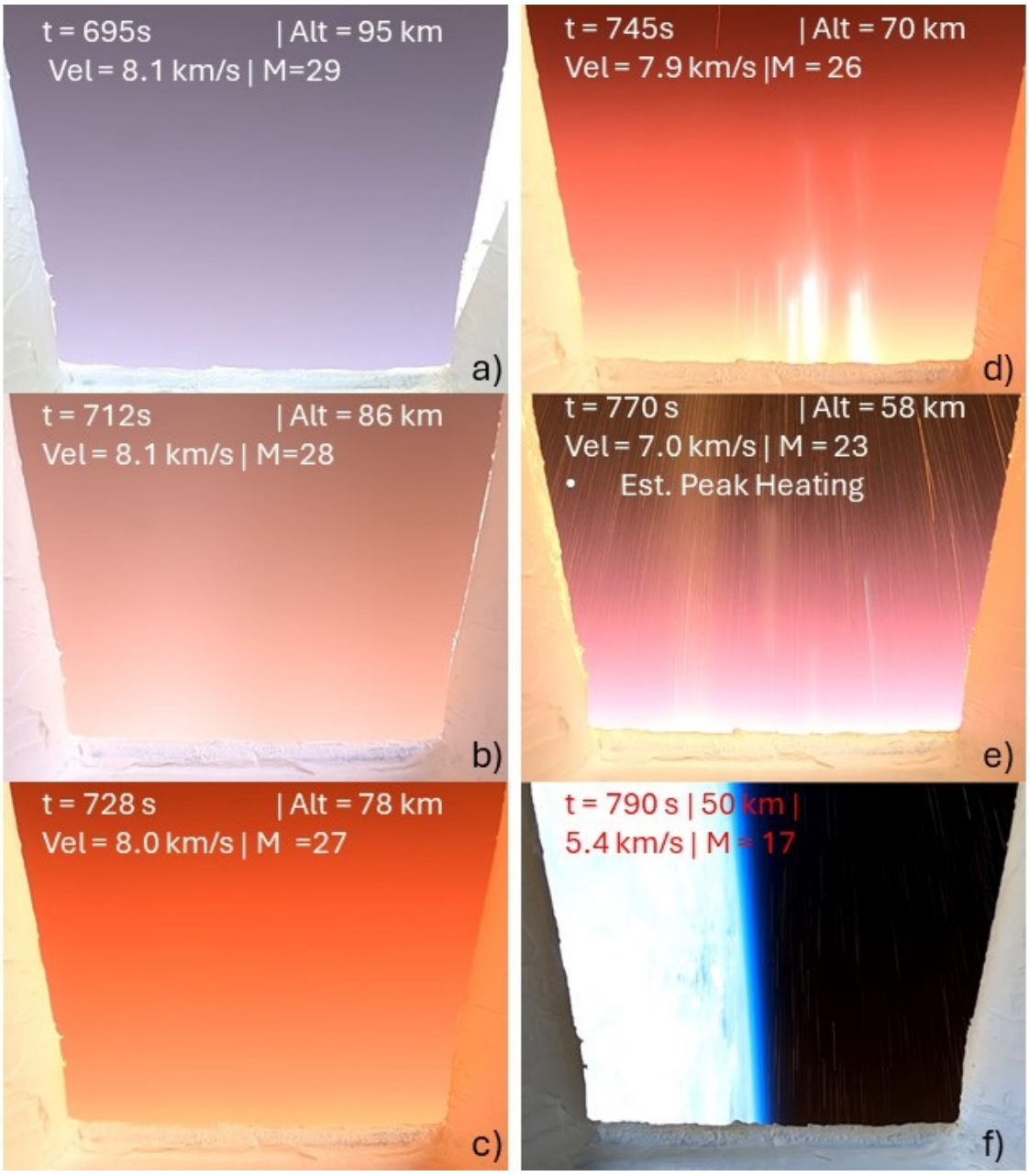

Fig. 3 Video observations from Varda's first hypersonic flight. A long video is available at [18].

purple glow over a period of approximately 100s. The vehicle heatshield ejected spallation products between 745 s and 770 s after separation. These products showed up as bright streaks in Fig. 3d and 3e. Although spallation might affect spectral measurements, these are expected to be transient and will be filtered out in the final data. Note that Fig. 3e highlights emissions that were observed while the vehicle was experiencing peak reentry heating and Fig. 3f highlights emissions emissions near the peak dynamic pressure trajectory point. The remainder of this paper will focus on simulating radiance and spectrometer response at these two trajectory points.

IV. CFD Flowfield Calculations

Table 1 Trajectory points simulated in LAURA for this study.

Case	Altitude (km)	v_∞ (m/s)	T_∞ (K)	q (kPa)	ρ_∞ (kg/m^3)
Peak Heating	58.03	6850	251.9	9.75	4.16E-04
Peak Dynamic Pressure	46.49	4440	269.4	16.6	1.69E-03

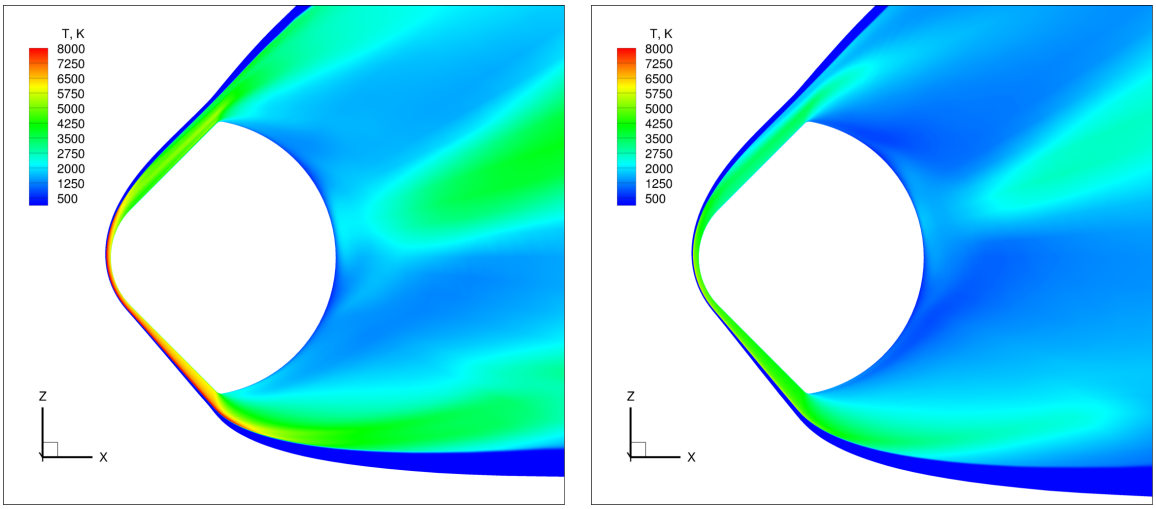

(a) **(b)**

Fig. 4 CFD flowfield solutions using the 11 species air-chemistry model for the Varda Hypersonic Testbed vehicle with α = 20° at a) peak heating and b) peak dynamic pressure.

Flowfield property calculations of the Varda Hypersonic Testbed vehicle were performed using LAURA with 5 species (N_2, O_2, NO, N, O) and 11 species (N_2, O_2, NO, N, O, N_2^+, O_2^+, NO^+, N^+, O^+, e^-) air chemistry models assuming thermal equilibrium and chemical nonequilibrium. The simulations used a simplified mesh geometry of the capsule that did not model the aftbody separation pockets. The spectrometer collimator actually sits within the separation pocket on the actual testbed to help reduce convective heat fluxes of the optics. The cross section of the actual vehicle is depicted in Fig. 1b. Two points of the reentry trajectory were investigated, corresponding to peak heating and peak dynamic pressure. Table 1 lists the relevant flight parameters for these conditions and these flight conditions can be seen visually in Fig. 3 e and f. The capsule aeroshell is designed to be self-stabilizing once it reaches the upper atmosphere; however, the vehicle angle of attack may initially oscillate as it stabilizes. Therefore, the presented work models the capsule at an angle-of-attack (α) of 0° and 20° in order to conservatively bound potential reentry oscillations. For the simulations, the viscous flow was assumed to be laminar and the surface of the capsule was treated as super-catalytic, radiative equilibrium walls . Ablation products were neglected in this study, while radiation in the flowfield was calculated using NEQAIR (Section IV).

Figure 4 shows the CFD flowfield solutions using an 11 species model for α = 20° at peak heating and peak dynamic pressure. The 5 species model flowfield is qualitatively identical to the 11 species model depicted here. At peak heating, the shock layer reached translational temperatures (T_{tr}) in excess of 13,000 K in the stagnation region, however in

temperature contours in Fig.4 are cut off at 8000 K for clarity. This region, as well as the shock-layer, mainly contribute to the dissociation of oxygen (O_2) and nitrogen (N_2). There is a large temperature gradient as the flow accelerates around the nose and shoulder of the vehicle, where atomic oxygen and nitrogen begin to recombine. There are two regions of separated flow around the shoulders with lower temperatures. The compression of flow near the windward side of the capsule leads to excessive temperatures compared to the leeward side, which, in turn, contributes to the increase of chemical dissociation on the windward side. The temperatures in the viscous wake are similar to those in the downstream shock-layer as the wake flow is further compressed.

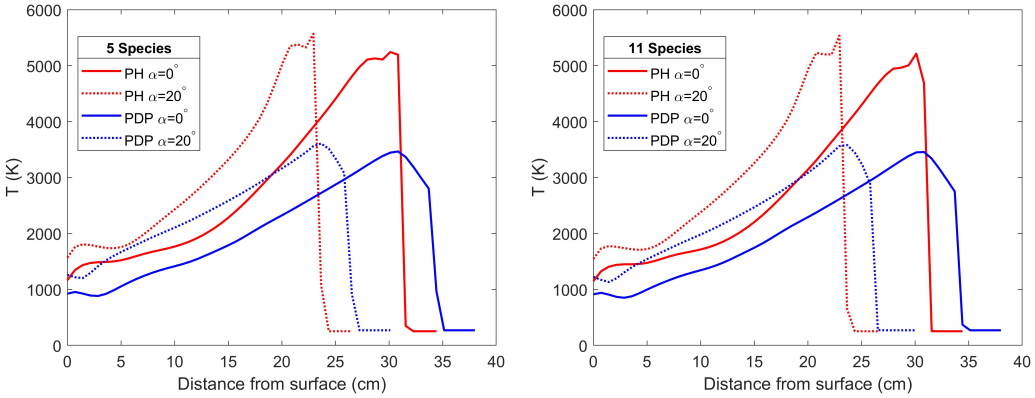

(a) **(b)**

Fig. 5 LOS temperature variation in the flowfield for a) peak heating and b) peak dynamic pressure using 11 species (dotted lines) and 5 species (solid lines) air chemistry models for α = 0° (blue) and 20° (red).

Figure 5 shows the temperature variation along the spectrometer LOS for the 11 and 5 species models. The shock layer remains above 5,000 K past the shoulder as it passes the LOS. The large volume of shock-heated air produces strong emissions that will be recorded by the spectrometer. Additionally, the flowfield temperature is significantly lower as the capsule descends through the atmosphere and decelerates, which his depicted in the peak dynamic pressure solutions in Fig. 5. The temperature in the stagnation region decreases to roughly 7,000 K at peak dynamic pressure (Fig. 4b). Consequently, the emitted radiance also decreases as the capsule descends through the atmosphere, which is accompanied by large variations in the specific atomic and molecular species present in the flow.

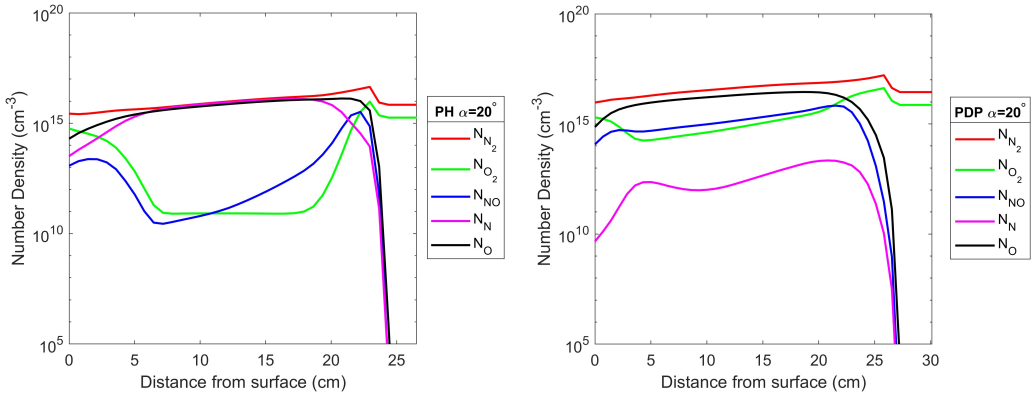

(a) **(b)**

Fig. 6 5 species number densities along LOS for a) peaking heating and b) dynamic pressure for α = 20°.

Figure 6a shows the 5 species model number densities at peak heating for α = 20°. At these conditions, the number density of N_2 rises less than a single order of magnitude along the LOS for both angles of attack and accounts for the majority of the total species' population in the flow. The number density of O_2 drops immediately after the vehicle surface and rises to peak values at roughly 30 cm for α = 0° and 25 cm for α = 20°, with a sharper increase to peak density at α = 20°. Both N and O species exhibit a gradual rise in density until the peak value, followed by a sharp

drop near the edge of the flowfield. NO exhibits lower densities and is concentrated near the vehicle and in the shock. Figure 6b shows the 5 species model number densities at peak dynamic pressure for $\alpha = 20°$. At this condition, the number density of N_2 again rises less than an order of magnitude along the LOS for both angles of attack and accounts for the majority of the total species' population in the flow. The number density of O_2 drops immediately after the vehicle surface and rises to peak values at roughly 35 cm for $\alpha = 0°$ and 25 cm for $\alpha = 20°$. The number densities of NO, N, and O increase near the surface of the vehicle and then drop off gradually towards the edge of the flowfield. The quantity of N is several orders of magnitude lower in the peak dynamic pressure flowfield than for the peak heating flowfield. The lower quantity of N_2 dissociation is due, in part, to the decreased temperature in the peak dynamic pressure flowfield. However, O_2 still readily dissociates at these conditions leading to an appreciable concentration of O and NO. Interestingly, the NO number density is higher at peak dynamic pressure than it is at peak heating.

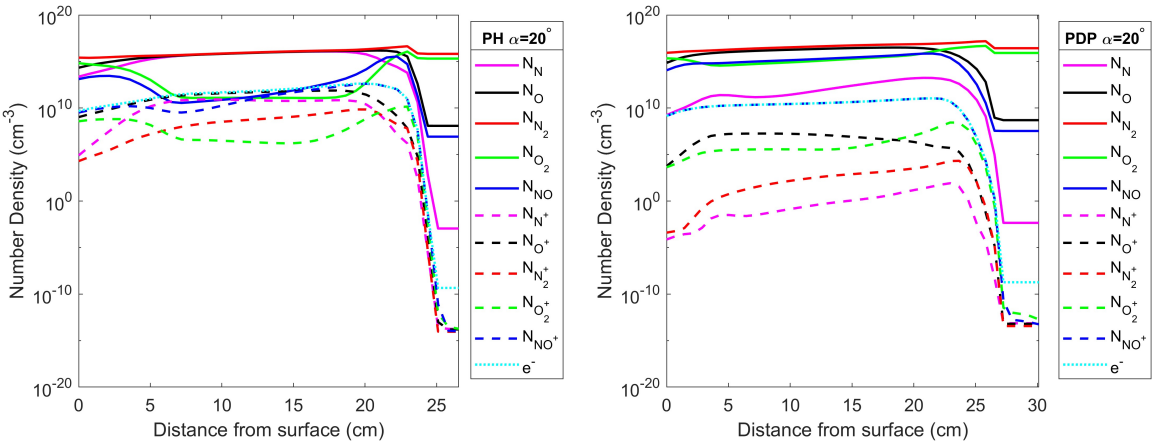

(a) **(b)**

Fig. 7 11 species number densities along LOS for a) peaking heating and b) dynamic pressure for $\alpha = 20°$.

Figure 7a shows the 11 species solution at peak heating for $\alpha = 20\ °$. At this condition, the number density of O_2 decreases by roughly 5 orders of magnitude between 5 and 20 cm from the surface of the vehicle. The O_2 number density then rises to a maximum just before sharply dropping off in the shock boundary, after which it levels out to freestream conditions. The number densities of NO and O_2^+ follow a similar trend, with the concentration of O_2^+ roughly 6 orders of magnitude less than NO and O_2. Conversely, the number densities of O and O^+ both increase by 2 orders of magnitude before decreasing within roughly 5 cm of the shock boundary, with the O^+ concentrations being 5 orders of magnitude less than O. The number densities of N_2, N_2^+, N, and N^+ depict a similar trend. N_2 rises an order of magnitude, N rises 3 orders of magnitude, and N_2^+ and N^+ rise 6 orders of magnitude each. All species concentrations sharply decrease when within roughly 5 cm of the edge of the shock boundary, then return to freestream conditions outside the shock layer. The ionized species (O^+, N^+, NO^+, O_2^+, N_2^+) concentrations are significantly lower compared to their neutral counterparts. These results, along with the presence of e^-, implies a strong dissociation of O_2 and N_2 into their constituent atoms, manifesting primarily in the bulk of the flowfield.

Figure 7b shows the 11 species solution at peak dynamic pressure for $\alpha = 20°$. For these conditions, the number density of O_2 decreases by an order of magnitude at roughly 3 cm from the edge of the vehicle, then rises 2 orders of magnitude until the edge of the shock boundary. The number density of N_2 shows a very gradual increase less than an order of magnitude between the edge of the vehicle and edge of the shock boundary. The number density of O^+ increases 3 orders of magnitude within the first 3 cm in the flowfield moving away from the edge of the vehicle, then gradually decreases by 2 orders of magnitude near the shock boundary. The number densities of N, NO, and NO^+ show a small increase of an order of magnitude near the surface of the vehicle, with NO^+ concentrations 5 orders of magnitude less than NO. The number density of N, N^+, and O_2^+ all show similar trends. These trends consist of a local maximum concentration at roughly 3 cm from the edge of the vehicle and a global maximum concentration near the edge of the shock boundary. The number density of N_2^+ does not quite show the same trend but still exhibits a sharp increase in concentration near 3 cm from the edge of the vehicle and a maximum concentration near the edge of the shock boundary. The number densities of NO^+ and e^- are nearly identical. Overall, the concentration of ionized species (O^+, N^+, NO^+, O_2^+, N_2^+) are lower than those observed at peak heating. The lower flowfield temperature at peak dynamic pressure

likely limits the occurrence of ionization, which is depicted by the reduced number density of ionized species.

V. Spectral Emission Predictions

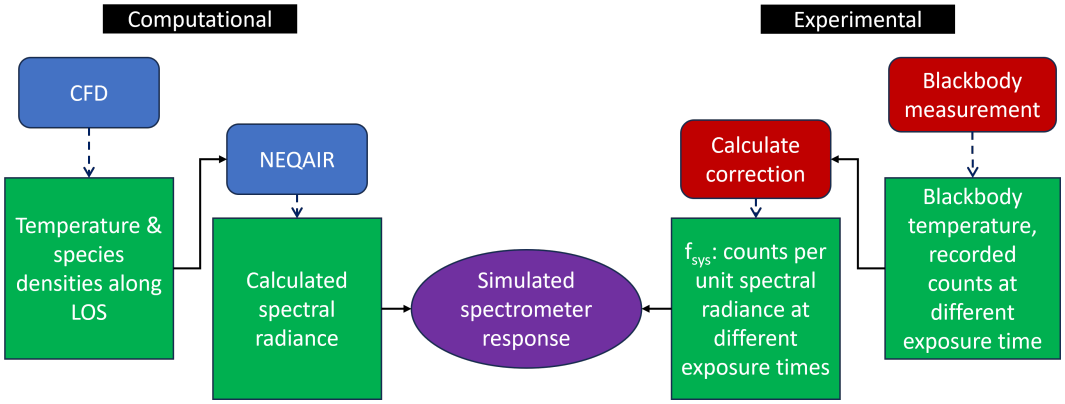

Fig. 8 Data flow for determining simulated spectrometer response using NEQAIR computed radiance and experimentally determined spectrometer conversion factor.

The data obtained from the CFD simulations was used to compute the emitted spectral radiance of the plasma sheath and determine the spectrometer response for different detector exposure times per the methodology in Figure 8. Once a converged flowfield solution was obtained, the LOS data points were extracted using Tecplot. This data included the flow temperature, the mass density, and the atomic, molecular, and electron (for 11 species runs) mass fractions recorded at every point along the LOS. Basic stoichiometric calculations were used to convert the species mass fractions into number densities and then generate an input data file containing the distance along the LOS, the total number density, the temperature, and the individual species number densities in separate columns. This LOS input file was fed into NEQAIR to calculate the spectral radiance along the LOS for wavelength values between 346.5 nm and 807.2 nm with a spectral grid spacing of 0.2184 nm. These numbers correspond to the wavelength range and resolution of the OSPREE payload. Since the flow around the capsule was assumed to be in state of chemical nonequilibrium, the atomic and molecular excited state populations could not be expected to follow a Boltzmann distribution. As a result, NEQAIR was run in its non-Boltzmann state population mode which uses a collisional-radiative (CR) interaction model to determine excited electronic state populations for each species. A spectrometer records intensity (measured in photon counts) rather than spectral radiance. To determine the sensor response from the calculated radiance, laboratory measurements of the spectra of a tungsten (blackbody) calibration lamp operating at 1800 K were taken with the flight spectrometer using 4 different exposure times: 25ms, 50ms, 100ms, and 250ms. Dividing the recorded spectrum at each exposure time by the Planck distribution function using T=1800 K for the provided wavelength range produced a set of system conversion factors to convert the NEQAIR computed spectral radiance to detector counts.

The spectral radiance calculated using NEQAIR for the peak heating and peak dynamic pressure trajectory points are plotted in Fig. 9a and 10a for the 5 species and 11 species models, respectively. For both air-chemistry models, the spectra are dominated by N_2 and NO emissions between 350-500 nm. Additionally, O_I emissions can be seen at 630 and 636 nm, which are more prevalent at peak dynamic pressure. In the 11 species model, an additional O_I emission at 777 nm is present that does not manifest in the emitted radiance calculated using the 5 species model input data. When implementing flowfield data from 11 species CFD models in NEQAIR and using non-Boltzmann state population, several new collisional and radiative interaction pathways are introduced with the addition of ionized species that are not present when using 5 species input data. Specifically, the contributions from free-bound collisions (electron and an O atom) could be contributing to the population of the electronic state which produces the 777 nm emission. Another major difference is that the spectral radiance calculated from the 5 species model flowfield data is 10-30% higher than that for the 11 species model, depending on the α and trajectory conditions. Careful inspection of Fig. 6 and 7 reveal that the 5 species models predict a slightly higher level of dissociation for O_2 and N_2 than the 11 species model. This likely is the origin of the higher predicted radiance from the 5 species model. Additionally, it seems that the ionic constituents of the 11 species model are of sufficiently low number densities that they do not contribute appreciably to the calculated radiance at this specific wavelength range. The radiance of the ionic species alone is 2 to 4 orders of

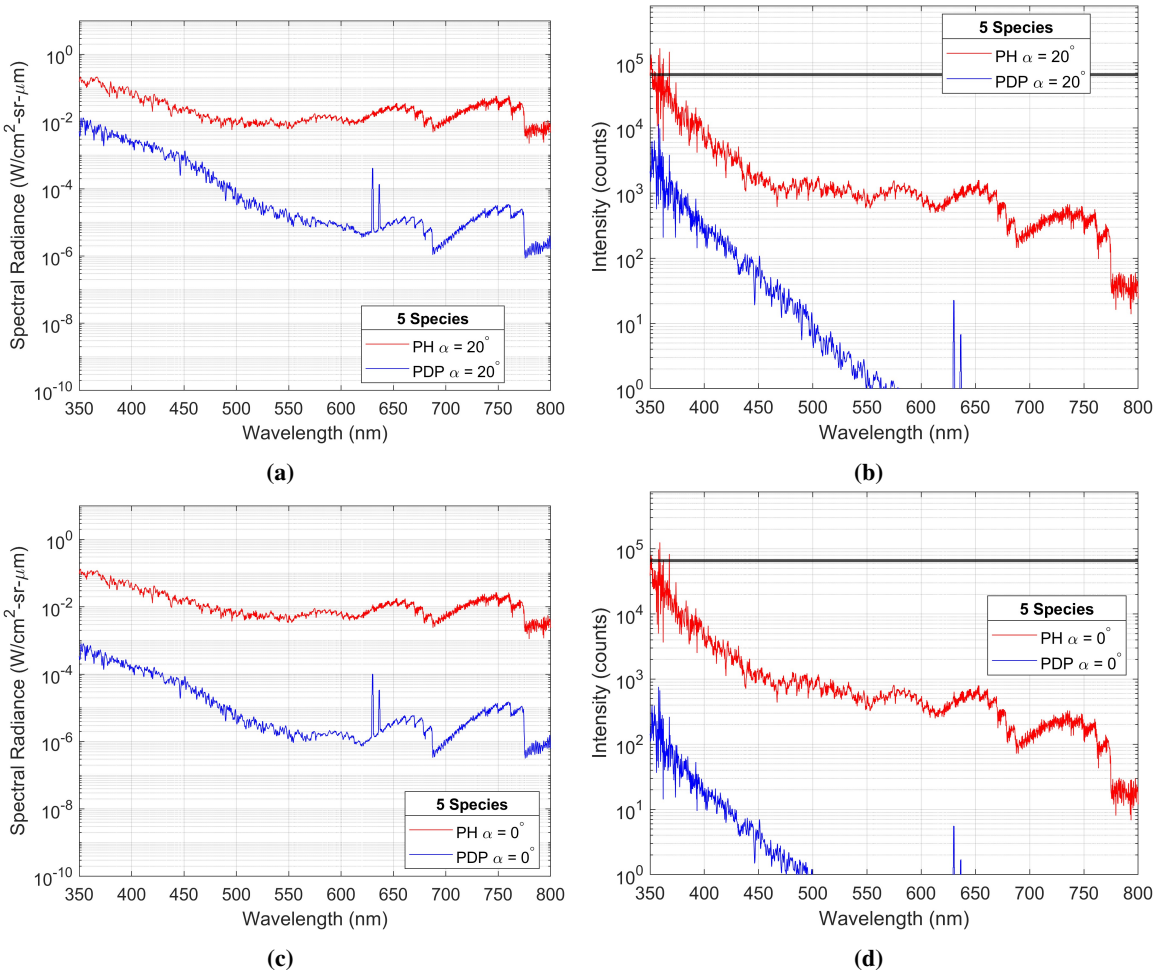

Fig. 9 Simulated spectral radiance for peak heating (blue) and peak dynamic pressure (red) using the 5 species air-chemistry model for a) $\alpha = 20°$ and c) $\alpha = 0°$. Predicted spectrometer response calculated from the simulated spectral radiance for peak heating and peak dynamic pressure using a detector exposure time of 100 ms for b) $\alpha = 20°$ and d) $\alpha = 0°$. The bolded black lines in b) and d) indicate the intensity at which the spectrometer detector saturates.

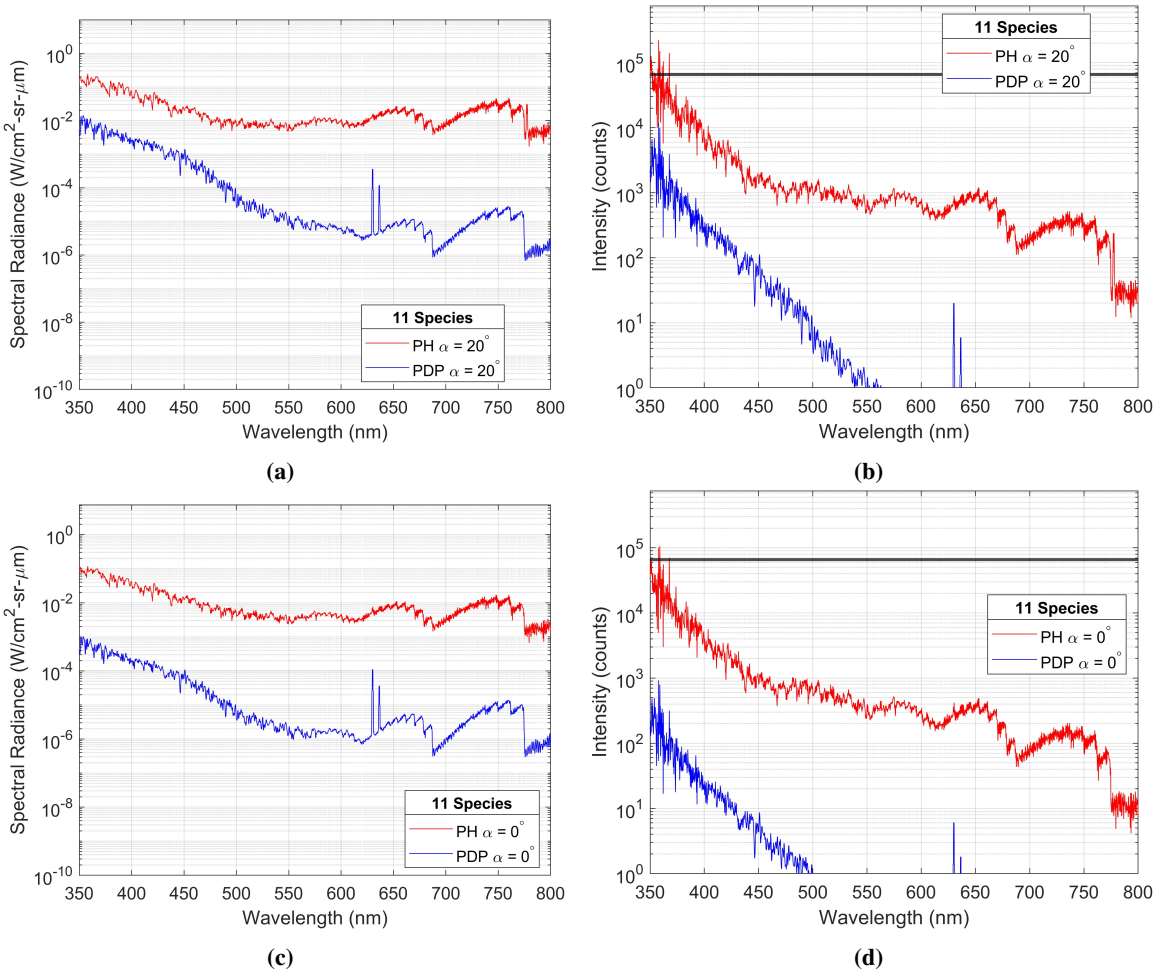

Fig. 10 Simulated spectral radiance for peak heating (blue) and peak dynamic pressure (red) using the 11 species air-chemistry model for a) $\alpha = 20°$ and c) $\alpha = 0°$. Predicted spectrometer response calculated from the simulated spectral radiance for peak heating and peak dynamic pressure using a detector exposure time of 100 ms for b) $\alpha = 20°$ and d) $\alpha = 0°$. The bolded black lines in b) and d) indicate the intensity at which the spectrometer detector saturates.

magnitude lower than that of the neutral species (not shown). However, given that the inclusion of ionic species and electronic open up pathways to new transitions, the 11 species model should be utilized to reproduce flight data.

The peak radiance drops 5 orders of magnitude between peak heating and peak dynamic pressure, indicating that changes in the flowfield during descent will drastically affect the emitted radiance and the signal measured by the spectrometer. The results in a concomitant decrease in the simulated spectrometer response, shown in Fig. 9b and 10b. The black line indicates the saturation point (65536 counts) of the detector; a correctly exposed signal lies within this bound. Figure 11 shows the spectrometer intensity as a function of detector exposure time from 25 to 250 ms. As expected, an increase in exposure time results in an increase in recorded signal intensity. Poor selection of exposure time for a given point in the trajectory can result in overexposure, in which the detector saturates, or underexposure, in which recorded emissions cannot be distinguished above noise. Moreover, as is evident in difference in intensity differences between peak heating and peak dynamic in Fig. 9 and 10, the spectral radiance will change drastically with trajectory and flight conditions. Thus, the simulated results indicate that the exposure time will need to be varied over the course of the trajectory in order to record spectra with a sufficient signal-to-noise ratio for adequate post-flight analysis and identification of strong emissions. Simulations for several points along the trajectory have been completed and the subsequent NEQAIR analysis was used to optimize the detector exposure time for a given point in the trajectory. These results will be presented in a subsequent publication detailing the spectrometer development.

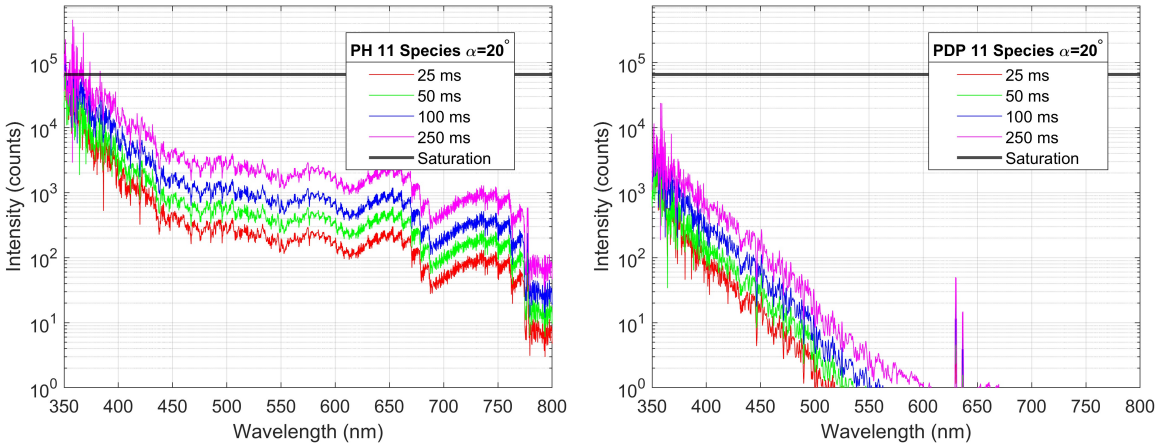

(a) **(b)**

Fig. 11 Predicted spectrometer response as function of exposure time from 25 to 250 ms for a) peak heating and b) peak dynamic pressure at α = 20°. The bolded black line indicates the intensity at which the spectrometer detector saturates.

VI. Conclusions

An analysis of the Varda Hypersonic Testbed vehicle has been conducted using the LAURA code in tandem with the NEQAIR radiation solver. Both 5 and 11 species air-chemistry models were utilized to simulate the flowfield. Results from the CFD simulations were used to calculate the spectral radiance along the LOS of OSPREE, an optical emission sensing payload. It was shown that the choice of air-chemistry model impacts the total spectral radiance minimally at the trajectory points studied, though additional transitions were observed for the 11 species models. In order to accurately reproduce the flight data, the 11 species model must be utilized in future comparisons. Moreover, it was found that the spectral radiance drops significantly between peak heating and peak dynamic pressure trajectory conditions. As such, the spectrometer detector exposure time will need to vary as the vehicle traverses the planned trajectory to best ensure correctly exposed spectral recordings. The results from this analysis have been used to develop the CONOPS of the OSPREE payload to be flown by AFRL in Varda's Hypersonic Testbed vehicle.

Acknowledgments

Distribution Unlimited; approved for public release under AFRL-2023-6241. The views expressed are those of the author(s) and do not necessarily reflect the official policy or position of the Department of the Air Force, the Department of Defense, or the U.S. government. This work was partially funded by an AFRL Edison grant, supporting the scientific objectives of a funded effort between Varda and the USAF under contract FA-9453-23-C-A035.

References

[1] Bertin, J. J., *Hypersonic aerothermodynamics*, AIAA, 1994.

[2] Ling, L., "OSIRIS-REx Off-Nominal Re-entry Breakup Analysis," *44th Annual AAS Guidance, Navigation and Control Conference*, 2022.

[3] Parkos, D., Alexeenko, A., Kulakhmetov, M., Johnson, B. C., and Melosh, H. J., "NOx production and rainout from Chicxulub impact ejecta reentry," *Journal of Geophysical Research: Planets*, Vol. 120, No. 12, 2015, pp. 2152–2168.

[4] Kulakhmetov, M. F., "Upscaling ab-initio chemistry models to non-equilibrium flow simulations," Ph.D. thesis, Purdue University, 2016.

[5] Kiefer, J. H., and Lutz, R. W., "The effect of oxygen atoms on the vibrational relaxation of oxygen," *Symposium (International) on Combustion*, Vol. 11, Elsevier, 1967, pp. 67–76.

[6] Kulakhmetov, M., Gallis, M., and Alexeenko, A., "Ab initio-informed maximum entropy modeling of rovibrational relaxation and state-specific dissociation with application to the O2+ O system," *The Journal of chemical physics*, Vol. 144, No. 17, 2016.

[7] Macdonald, R., Jaffe, R., Schwenke, D., and Panesi, M., "Construction of a coarse-grain quasi-classical trajectory method. I. Theory and application to N2–N2 system," *The Journal of chemical physics*, Vol. 148, No. 5, 2018.

[8] Gang Kim, J., and Boyd, I. D., "State-resolved thermochemical nonequilibrium analysis of hydrogen mixture flows," *Physics of Fluids*, Vol. 24, No. 8, 2012.

[9] Erdman, P. W., Zipf, E. C., Espy, P., Howlett, C. L., Levin, D. A., Collins, R. J., and Candler, G. V., "Measurements of ultraviolet radiation from a 5-km/s bow shock," *Journal of Thermophysics and Heat Transfer*, Vol. 8, No. 3, 1994, pp. 441–446.

[10] Kossi, K. K., and Boyd, I. D., "Detailed computation of ultraviolet spectra in rarefied hypersonic flow," *Journal of spacecraft and rockets*, Vol. 35, No. 5, 1998, pp. 653–659.

[11] Boyd, I., Phillips, W., Levin, D., Boyd, I., Phillips, W., and Levin, D., "Sensitivity studies for prediction of ultra-violet radiation in nonequilibrium hypersonic bow-shock waves," *35th Aerospace Sciences Meeting and Exhibit*, 1997, p. 131.

[12] Bose, D., and Candler, G. V., "Advanced model of nitric oxide formation in hypersonic flows," *Journal of thermophysics and heat transfer*, Vol. 12, No. 2, 1998, pp. 214–222.

[13] Lein, S., Reimer, T., Stubicar, K., Deuble, F., Auweter-Kurtz, M., Herdrich, G., and Winter, M., "Development of the re-entry spectrometer RESPECT for the ESA capsule EXPERT," *Acta Astronautica*, Vol. 64, No. 4, 2009, pp. 416–426.

[14] Winter, M., Fertig, M., and Auweter-Kurtz, M., "Status of the Re-Entry Spectrometer System RESPECT as a Payload on the European Re-Entry Capsule EXPERT," *4th International Symposium Atmospheric Reentry Vehicles and Systems, Arcachon, France*, 2005.

[15] Lein, S., Steinbeck, A., Preci, A., Fertig, M., Herdrich, G., Röser, H.-P., and Auweter-Kurtz, M., "Final Design and Performance Parameters of the Payloads PYREX, PHLUX and RESPECT on EXPERT," *Transactions of the Japan Society for Aeronautical and Space Sciences, Aerospace Technology Japan*, Vol. 8, No. ists27, 2010, pp. Tm_41–Tm_47.

[16] LAURA, *Langley Aerothermodynamic Upwind Relaxation Algorithm*, Software Package, Ver. 5.6, NASA Langley Research Center Hampton, VA, 2020.

[17] NEQAIR, *Nonequilibrium Radiative Transport and Spectra Program*, Software Package, Ver. 15.1, NASA Langley Research Center Hampton, VA, 2021.

[18] Varda, "Varda Capsule Reentry - Full Video from LEO to Earth," `https://youtu.be/BWxl921rMgM?si=KXp1-3YJzX-oZm7K`, 2024.